

HI AND CO VELOCITY DISPERSIONS IN NEARBY GALAXIES

K.M. MOGOTSI¹, W.J.G. DE BLOK^{2,1,3}, A. CALDÚ-PRIMO⁴, F. WALTER⁴, R. IANJAMASIMANANA⁵, A.K. LEROY^{6,7}

Draft version May 8, 2018

ABSTRACT

We analyze the velocity dispersions of individual HI and CO profiles in a number of nearby galaxies from the high-resolution HERACLES CO and THINGS HI surveys. Focusing on regions with bright CO emission, we find a CO dispersion value $\sigma_{\text{CO}} = 7.3 \pm 1.7 \text{ km s}^{-1}$. The corresponding HI dispersion $\sigma_{\text{HI}} = 11.7 \pm 2.3 \text{ km s}^{-1}$, yielding a mean dispersion ratio $\sigma_{\text{HI}}/\sigma_{\text{CO}} = 1.4 \pm 0.2$, independent of radius. We find that the CO velocity dispersion increases towards lower peak fluxes. This is consistent with previous work where we showed that when using spectra averaged (“stacked”) over large areas, larger values for the CO dispersion are found, and a lower ratio $\sigma_{\text{HI}}/\sigma_{\text{CO}} = 1.0 \pm 0.2$. The stacking method is more sensitive to low-level diffuse emission, whereas individual profiles trace narrow-line, GMC-dominated, bright emission. These results provide further evidence that disk galaxies contain not only a thin, low velocity dispersion, high density CO disk that is dominated by GMCs, but also a fainter, higher dispersion, diffuse disk component.

Subject headings: galaxies: ISM; ISM: molecules; radio lines: galaxies

1. INTRODUCTION

Gas velocity dispersions can be used to estimate the kinetic and thermal gas temperatures; to determine the mass distribution and structure of galaxies (e.g., Petric & Rupen 2007), and the stability, scale height and opacity of the gas disk. Velocity dispersions are important in studies of star formation, turbulence, the interstellar medium (ISM), and dynamics of galaxies. This is especially true of the vertical velocity dispersion σ_z . The rotation of the galactic disk has no effect on this component of the observed dispersion, and this makes it a useful parameter for studying the vertical structure of galactic disks. Dispersions are used to determine the stability of galactic disks against gravitational collapse using the Toomre parameter (Toomre 1964; Kennicutt 1989). Another link to star formation and turbulence studies is that dispersions can be used to determine the energy of the ISM (e.g., Agertz et al. 2009; Tamburro et al. 2009). They are also important in determining the midplane pressure of the gas disk (Elmegreen 1989; Leroy et al. 2008) and in star formation laws that consider a variable disk free-fall time (Elmegreen 1989; Krumholz & McKee 2005; Leroy et al. 2008). Larson (1981) used small-scale internal velocity dispersions to determine that molecular clouds are dominated by turbulent motions. Studies at larger scales can be used to determine the level of turbu-

lence found between giant molecular clouds and in large scale motions of gas in galaxies.

Studies of velocity dispersions require high spatial and velocity resolution observations (for vertical velocity dispersion studies, galaxies of low inclination are required so as to minimize the contribution from the radial and azimuthal dispersion components). The effective dispersion (σ_{eff}) can be thought of as a combination of the thermal broadening (v_t) and turbulent dispersion (σ_t):

$$\sigma_{\text{eff}}^2 = v_t^2 + \sigma_t^2 \quad (1)$$

(e.g., Agertz et al. 2009). The turbulent component can be decomposed into a radial (σ_r), angular (σ_ϕ), and vertical (σ_z) component, or a planar (σ_{xy}) and vertical component (σ_z). Theory and simulations show that the velocity dispersion is expected to be anisotropic, with $\sigma_r > \sigma_\phi > \sigma_z$ and $\sigma_{xy} \sim 2\sigma_z$ (Ageretz et al. 2009). When the beam of a telescope is large compared to the rotational velocity gradient in the observed galaxy (e.g., in high-redshift galaxies and highly inclined galaxies), beam smearing can affect the measured dispersion. For gas components with a clumpy structure (e.g., molecular gas), there are additional complications: the observed dispersion σ_{obs} is then a combination of the dispersion between clouds (cloud-cloud dispersions σ_{c-c}) and the internal velocity dispersion within the clouds (σ_{internal}):

$$\sigma_{\text{obs}}^2 = \sigma_{c-c}^2 + \sigma_{\text{internal}}^2 \quad (2)$$

The structure of HI is more filamentary and less clumpy than that of molecular gas. Its velocity dispersion is therefore generally not decomposed into internal and cloud-cloud components.

1.1. HI velocity dispersions

Since HI is the dominant gas component of galaxies and is easily observable through the 21 cm emission line, it has been extensively studied. HI velocity dispersions of nearby galaxies have been well studied, most notably by Petric & Rupen (2007) and Tamburro et al. (2009). Early work showed that $\sigma_{\text{HI}} \sim 6 - 13 \text{ km s}^{-1}$

¹ Astrophysics, Cosmology and Gravity Centre, Department of Astronomy, University of Cape Town, Private Bag X3, Rondebosch 7701, South Africa

² Netherlands Institute for Radio Astronomy (ASTRON), Postbus 2, 7990 AA Dwingeloo, the Netherlands

³ Kapteyn Astronomical Institute, University of Groningen, P.O. Box 800, 9700 AV Groningen, the Netherlands

⁴ Max-Planck-Institut für Astronomie, Königstuhl 17, D-69117, Heidelberg, Germany

⁵ College of Graduate Studies, University of South Africa, P.O. Box 392, UNISA, 0003, South Africa

⁶ Department of Astronomy, The Ohio State University, McPherson Laboratory, 140 West 18th Avenue, Columbus OH, 43210-1173, USA

⁷ National Radio Astronomy Observatory, 520 Edgemont Road, Charlottesville, VA 22903, USA

¹ email: moses.mogot@gmail.com

(e.g., Shostak & van der Kruit 1984, van der Kruit & Shostak 1984, Kamphuis & Sancisi 1993), with the dispersions dropping with increasing radial distance from the center (e.g., Kamphuis & Sancisi 1993). Hunter et al. (2001) and Hunter et al. (2011) also studied σ_{HI} in dwarf galaxies. Petric & Rupen (2007) performed high-resolution and high-sensitivity HI observations of the nearly face-on galaxy NGC 1058 to study its gas velocity dispersion. They found a vertical velocity dispersion of $4 - 14 \text{ km s}^{-1}$, which decreased with radius. These studies reached resolutions of $\sim 600 \text{ pc}$. Tamburro et al. (2009) used high-resolution HI data from The HI Nearby Galaxies Survey (THINGS; Walter et al. 2008) to study HI velocity dispersions. They also found that the dispersions decreased with radius. They found a mean σ_{HI} of $\sim 10 \text{ km s}^{-1}$ at r_{25} , dropping off to $\sim 5 \pm 2 \text{ km s}^{-1}$ at larger radii. Stacking analysis was used by Ianjamasimanana et al. (2012) to study the velocity dispersions averaged over HI disks of the THINGS galaxies. They found $\sigma_{\text{HI}} = 12.5 \pm 3.5 \text{ km s}^{-1}$ ($\sigma_{\text{HI}} = 10.9 \pm 2.1 \text{ km s}^{-1}$ for galaxies with inclinations less than 60°). This stacking analysis allowed them to study the HI velocity profiles at high signal-to-noise, enabling them to decompose the HI profiles into broad and narrow components. Fitting these components with Gaussians, they found $\sigma_{\text{HI}} = 6.5 \pm 1.5 \text{ km s}^{-1}$ for the narrow (cold) HI component and $\sigma_{\text{HI}} = 16.8 \pm 4.3 \text{ km s}^{-1}$ for the broad (warm) HI component. A similar analysis by Stilp et al. (2013) of partially the same data found velocity dispersions of the bulk of the HI of $\sim 6 - 10 \text{ km s}^{-1}$.

1.2. CO velocity dispersions

CO velocity dispersions have been less studied than those of HI. Mostly this has been due to technical limitations. Early observations of the lowest three CO rotational transitions found dispersions in the range of $5 - 9 \text{ km s}^{-1}$ (Stark 1984; Wilson & Scoville 1990; Combes & Becquaert 1997; Walsh et al. 2002; Wilson et al. 2011). Recent instrumental developments have enabled more extensive studies of the CO distribution in galaxies, such as the HERA CO Line Extragalactic Survey (HERACLES; Leroy et al. 2009); see also Section 2. HERACLES is a CO $J = 2 \rightarrow 1$ survey of nearby galaxies, covering their entire star-forming disks. It partially overlaps with the THINGS survey, meaning HI and CO data are available at comparable resolutions.

Caldú-Primo et al. (2013) used data from HERACLES and THINGS to compare CO and HI velocity dispersions as averaged over large areas using the stacking technique. They analyzed the dispersions of these stacked HI and CO velocity profiles, stacking by galactocentric radius, star formation, HI, CO and total gas density. They found that $\sigma_{\text{HI}} = 11.9 \pm 3.1 \text{ km s}^{-1}$, $\sigma_{\text{CO}} = 12.0 \pm 3.9 \text{ km s}^{-1}$ with $\sigma_{\text{HI}}/\sigma_{\text{CO}} = 1.0 \pm 0.2$. In other words, the CO dispersions they found are very similar to the HI dispersions. Caldú-Primo et al. (2013) suggested that this indicates the presence of an additional, more diffuse, higher dispersion molecular disk component that is similar in thickness to the HI disk (see also Shetty et al. 2014). This finding is in agreement with independent studies by, e.g., Garcia-Burillo et al. (1992) who find, in addition to a thin molecular disk, a 2–3 kpc thick molecular “halo” around the edge-on galaxy NGC 891. A similar thick molecular disk is also found by Combes et al. (2012) in M33. Pety

TABLE 1
NOISE AND VELOCITY RESOLUTION OF THE HI AND CO CUBES.

Galaxy	HI Noise [mJy beam ⁻¹]	CO Noise [mK]	HI ΔV [km s ⁻¹]	CO ΔV [km s ⁻¹]
(1)	(2)	(3)	(4)	(5)
NGC 628	0.60	21	2.6	5.2
NGC 925	0.57	16	2.6	5.2
NGC 2403	0.38	19	5.2	5.2
NGC 2841	0.35	16	5.2	5.2
NGC 2903	0.41	21	5.2	5.2
NGC 2976	0.36	20	5.2	5.2
NGC 3184	0.36	17	2.6	5.2
NGC 3198	0.33	17	5.2	5.2
NGC 3351	0.35	19	5.2	5.2
NGC 4214	0.69	19	1.3	5.2
NGC 4736	0.33	21	5.2	5.2
NGC 5055	0.36	26	5.2	5.2
NGC 6946	0.55	25	2.6	5.2

NOTE. — Column 1: Galaxy name; Column 2: Noise per channel in HI data; Column 3: Noise per channel in CO data; Column 4: HI velocity resolution; Column 5: CO velocity resolution.

et al. (2013) compared interferometric and single-dish observations of M51 (NGC 5194) and also found evidence of an extended molecular disk. Similar results have been found by Caldú-Primo et al. (2015), again by comparing interferometric and single-dish imaging of the molecular gas disks in nearby galaxies.

The results presented in Caldú-Primo et al. (2013) were based on stacked profiles, i.e., profiles averaged over large regions. In this paper we use the same THINGS and HERACLES data as used by Caldú-Primo et al. (2013) to determine whether evidence for the diffuse molecular component can also be found in individual profiles. In particular, we investigate whether the velocity dispersion of the CO profiles changes as a function of CO intensity, which is what one would expect if a diffuse, high-velocity dispersion component is indeed present.

In Section 2 we describe the data used. Section 3 contains a description of the results of our analysis. Section 4 contains a discussion of our results and a comparison to other work. In Section 5 we summarize our conclusions.

2. DATA AND METHOD

We used Hanning-smoothed CO data cubes from HERACLES (Leroy et al. 2009), which is a molecular gas survey of nearby galaxies using the HERA receiver array on the IRAM 30-m telescope.¹ For the neutral hydrogen, we used residual-scaled natural-weighted HI data cubes from THINGS (Walter et al. 2008), which is a 21-cm survey of 34 nearby spiral and dwarf galaxies. The observations were done with the NRAO² Jansky Very Large Array. The work in this paper is based on the analysis done on 13 galaxies (see Table 1) that are common to both surveys and which have CO detections. The properties of these galaxies can be found in Table 1 of Walter et al. (2008). For convenience, noise values and velocity resolutions of the HI and CO observations are listed in Table 1. Note that these are the same data as used in the analysis presented in Caldú-Primo et al. (2013).

¹ IRAM is supported by CNRS/INSU (France), the MPG (Germany), and the IGN (Spain)

² The National Radio Astronomy Observatory is a facility of the National Science Foundation operated under cooperative agreement by Associated Universities, Inc.

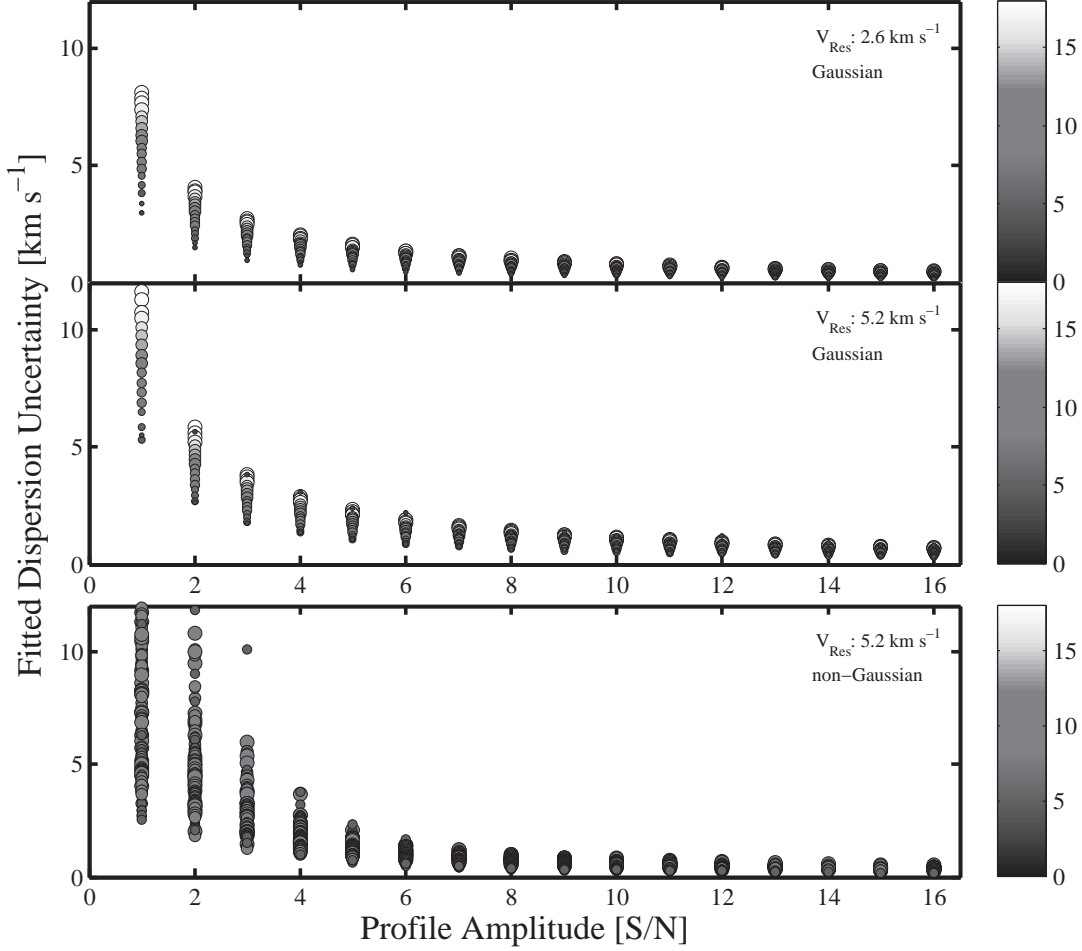


FIG. 1.— Uncertainties in fitted dispersions (y-axis) for Gaussian profiles of various amplitudes and dispersions. The input Gaussian amplitudes (in signal-to-noise units) are shown on the x-axis. Marker sizes and grayscale represent input velocity dispersions. *Top and middle panels:* Gaussian velocity profiles were added to random Gaussian noise and Gaussians were fitted to the resultant velocity profiles. The mean of 1000 iterations is plotted for each input amplitude and dispersion value. The y-axis values are the mean uncertainties of the fitted dispersions. The top panel is for simulated data with a velocity resolution of 2.6 km s^{-1} ; the middle panel is for a resolution of 5.2 km s^{-1} . *Bottom panel:* Gaussian velocity profiles were added to real noise extracted from 5.2 km s^{-1} resolution CO data cubes and Gaussians were fitted to the resultant velocity profiles. The noise from the cubes was selected from regions with no galactic emission.

The CO data generally have a spatial resolution of $13''$. The natural-weighted HI data cubes mostly have resolutions better than this, but were smoothed to $13''$ to match the resolution of the CO data.

A number of recent studies of HI velocity profiles have used Gauss-Hermite profiles to take into account asymmetries in the profiles or used multiple Gaussian components to quantify the presence of different components of the ISM (e.g., de Blok et al. 2008, Ianjamasimanana et al. 2012). We did explore these fitting functions for our profiles, but found that the CO profiles are better described by simple, single Gaussians. In order to minimize the number of fit parameters, and as we are only interested in the general width of the profile, we therefore use single Gaussians to fit both the HI and CO profiles.

In fitting the profiles we imposed a $4S$ noise cutoff on the fitted peak fluxes of the profiles, where S is the rms noise of the profile.³ Only positions where both HI and CO profiles had peak fluxes greater than $4S$ were retained. For the HI data, determining the $4S$ values was

³ To avoid confusion with the velocity dispersion σ , we use S throughout this paper to indicate the rms noise level.

done using non-residual-scaled cubes, as residual-scaling affects the relation between signal and noise (see Walter et al. 2008 for a full description of the residual scaling procedure). These results were then applied as a mask to the residual-scaled cubes. The remaining velocity profiles of these masked residual-scaled cubes were then fitted and analyzed. In addition to the peak-flux criterion, we also imposed a velocity resolution cutoff where all profiles with fitted dispersions smaller than the velocity resolution of their data cube were removed.

We simulated how the uncertainties in the fitted dispersions behave by producing random Gaussian noise at velocity resolutions relevant to our data, adding predetermined Gaussian velocity profiles to them and re-fitting the data. Simulations were performed with input Gaussian profiles of different amplitudes and dispersions. A thousand iterations of data simulation and fitting were performed for each input amplitude and dispersion value. This was done for different velocity resolutions and the averages of the fit uncertainties are plotted in Fig. 1 (top and middle panel). Input dispersions ranged between 2.6 km s^{-1} and 20 km s^{-1} .

For velocity profiles with peak fluxes greater than $4S$ and velocity resolutions of 2.6 km s^{-1} , the mean uncertainties in the fitted dispersion were smaller than $\sim 2 \text{ km s}^{-1}$. For velocity profiles with peak flux equal to $4S$ and velocity resolutions of 5.2 km s^{-1} , the mean errors in the fitted dispersion were between 1.4 km s^{-1} and $\sim 3 \text{ km s}^{-1}$.

A small number of the CO spectra showed some minor baseline ripples resulting in a slightly non-Gaussian noise behaviour. We therefore repeated the same procedure but added noise extracted from these CO cubes rather than random Gaussian noise. This was done for profiles with peak values between $1S$ and $16S$. The results are plotted in Fig. 1 (bottom panel). The results for the CO noise simulation are consistent with the results from the Gaussian noise simulation down to $4S$ peak flux levels.

3. RESULTS

3.1. Comparing HI and CO velocity dispersions

Using the results from the Gaussian fits, HI and CO dispersion maps were made for each galaxy. In addition, we made dispersion difference ($\sigma_{\text{CO}} - \sigma_{\text{HI}}$) and dispersion ratio ($\sigma_{\text{HI}}/\sigma_{\text{CO}}$) maps for each galaxy by taking the CO and HI dispersion maps and then doing a pixel-by-pixel subtraction or division.

The dispersions were binned into 1 km s^{-1} bins. Histograms of the σ_{HI} and σ_{CO} distributions for those positions in each galaxy where HI and CO were both present are shown in Figs. 2 and 3. The distribution of dispersion values from pixels outside the central $0.2r_{25}$ and with small fit uncertainties ($\Delta\sigma \leq 1.5 \text{ km s}^{-1}$) are shown as the shaded histograms in the figures. The $0.2r_{25}$ selection was used in order to minimize the effect of beam smearing, as discussed later in this section. Dispersions are plotted against the number of resolution elements (defined as the ratio of the number of pixels and the number of pixels per beam), or, equivalently, the number of beams. From the histograms it is clear that in regions where there is both HI and CO emission, σ_{HI} values range from $\sim 5 - 30 \text{ km s}^{-1}$ and σ_{CO} values range from $\sim 5 - 25 \text{ km s}^{-1}$. The σ_{HI} modes range from $9 - 22 \text{ km s}^{-1}$ and σ_{CO} modes range from $6 - 15 \text{ km s}^{-1}$ (see Table 2). Most of the high dispersions have large fitting errors and/or are from pixels in the central regions of galaxies, as shown in Figs. 2 and 3. Such large dispersions are usually due to multiple gas components in the line of sight and/or beam smearing. These give non-Gaussian profiles resulting in bad fits.

The σ_{HI} distributions clearly peak at values much larger than the dispersion cutoffs imposed due to the velocity resolution of the data. However, many of the σ_{CO} distributions have peaks near the dispersion cutoffs. In a few cases clear σ_{CO} distribution peaks are not seen (e.g., NGC 2403), and therefore the true mean (and mode) σ_{CO} values for these galaxies are likely to be smaller than 5.2 km s^{-1} .

The incomplete sampling and asymmetry of the velocity dispersion histograms means that, especially for the CO, the mean is not a good statistic to characterize the distribution (it will overestimate the typical dispersion value). We therefore also use the mode to describe the dispersion distributions. The modes were calculated after binning the dispersions using a 1 km s^{-1} bin size. The

values are listed in Table 2.

Most of the σ_{CO} modes range from 6 to 11 km s^{-1} (12/13 galaxies) while their means range from 7 to 15 km s^{-1} (11/13 galaxies); most of the σ_{HI} modes range from 9 to 17 km s^{-1} (12/13 galaxies) and their means range from 9 to 21 km s^{-1} (11/13 galaxies). NGC 2841, NGC 2903, NGC 3198 and NGC 3351 were not included in the determination of the average values due to their high inclinations and very asymmetric dispersion distributions. The average σ_{CO} mode is $7.3 \pm 1.7 \text{ km s}^{-1}$ (average of the σ_{CO} means is $10.5 \pm 3.6 \text{ km s}^{-1}$), and the average σ_{HI} mode is $11.7 \pm 2.3 \text{ km s}^{-1}$ (average of the σ_{HI} means is $14.1 \pm 4.3 \text{ km s}^{-1}$). Characteristic values of σ_{HI} and σ_{CO} are listed in Table 3. We also list the median values there for comparison with results from Caldú-Primo et al. (2013) which were derived from stacking the same data we use (see Section 4).

We constructed histograms of the $\sigma_{\text{CO}} - \sigma_{\text{HI}}$ values using bins of 1 km s^{-1} . For the $\sigma_{\text{HI}}/\sigma_{\text{CO}}$ data we made histograms using bins of size 0.2. Figure 4 shows the $\sigma_{\text{CO}} - \sigma_{\text{HI}}$ distributions for each of the galaxies. Figure 5 shows the $\sigma_{\text{HI}}/\sigma_{\text{CO}}$ distributions. These all have Gaussian shapes and are symmetric and well-sampled. We therefore fitted Gaussians to the distributions. The fitted mean dispersion difference and ratios are shown in Table 2. The CO distribution in NGC 925 and NGC 4214 only encompasses a few resolution elements and care should be taken when interpreting their fits. The mean $\sigma_{\text{CO}} - \sigma_{\text{HI}}$ value is $-3.3 \pm 1.2 \text{ km s}^{-1}$; the mean $\sigma_{\text{HI}}/\sigma_{\text{CO}}$ is 1.4 ± 0.2 . A summary of the mean, modes, and medians of the dispersion values is shown in Table 3.

Caldú-Primo et al. (2013) quantified the effect of beam smearing in our galaxies by simulating spiral galaxies with 30° , 60° , and 80° inclinations. They found that beam smearing is greatest in the central regions of galaxies and in highly inclined galaxies. The observed dispersion can be increased by at most a factor of 1.2 at $0.2r_{25}$ for galaxies with 30° inclination, 1.5 for 60° , and 1.8 for 80° , with these factors decreasing quickly toward unity at larger radii. They therefore used an $0.2r_{25}$ radial cut-off for their analysis. Even though Figures 2 and 3 and Table 4 show that including the inner pixels does not greatly affect our conclusions, in our radial analysis and distribution width analysis we only use pixels with radii greater than $0.2r_{25}$ which are therefore not affected by beam smearing.

Our σ_{HI} values are in agreement with Leroy et al. (2008) ($\sigma_{\text{HI}} = 11 \pm 3 \text{ km s}^{-1}$), Ianjamasimanana et al. (2012) ($\sigma_{\text{HI}} = 12.5 \pm 3.5 \text{ km s}^{-1}$) and Caldú-Primo et al. (2013) ($\sigma_{\text{HI}} = 11.9 \pm 3.1 \text{ km s}^{-1}$) who all analyzed the THINGS galaxies.

We also studied radial trends of the dispersions. The radial σ_{HI} , σ_{CO} and $\sigma_{\text{HI}}/\sigma_{\text{CO}}$ distributions are shown in Figs. 6 and 7. These plots were made using annuli where the filling factors were higher than 10% and 25%, respectively. In our analysis we use the results from the 10% annuli. Comparison with the 25% annuli shows that this choice of filling factor has little effect on our results. The $\sigma_{\text{HI}}/\sigma_{\text{CO}}$ values in this analysis were calculated by azimuthally averaging the $\sigma_{\text{HI}}/\sigma_{\text{CO}}$ maps.

Figure 6 shows σ_{CO} and σ_{HI} decreasing with radius for most of the galaxies. These also flatten off at larger radii.

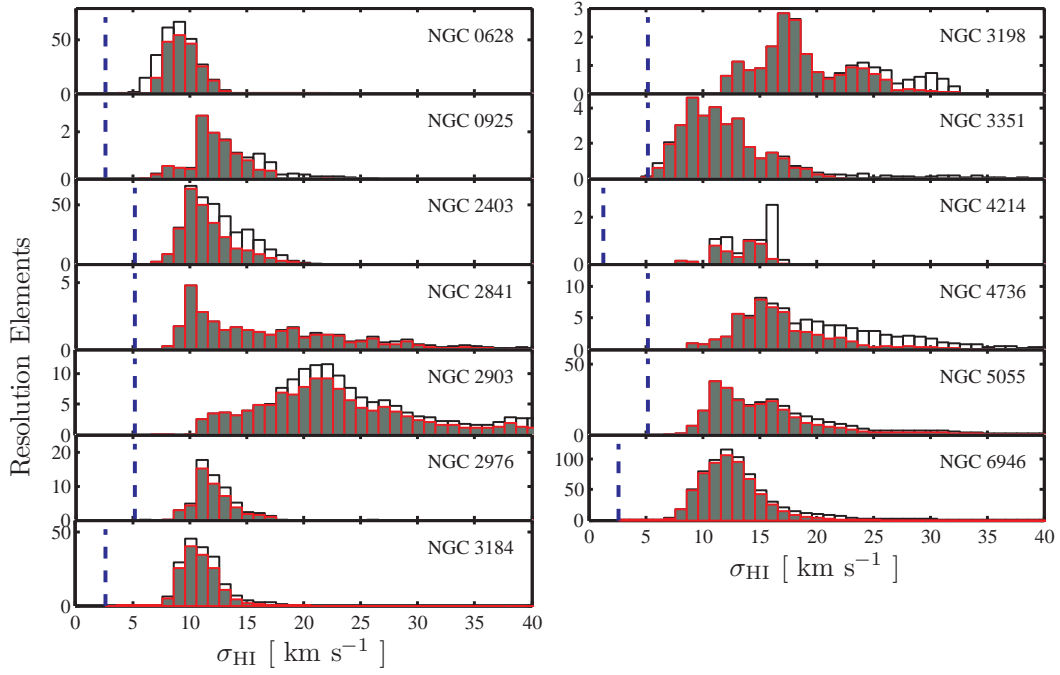


FIG. 2.— Distributions of the H I dispersions σ_{HI} for positions that have both CO and H I emission. The velocity dispersion cutoffs are indicated by the vertical dotted lines. The y-axis is in resolution elements (resolution elements = [number of pixels]/[number of pixels per single resolution element], i.e. number of beams). Open bars show the distribution for all profiles. The gray shaded bars with red outlines show the distribution of dispersions for profiles with a fit uncertainty less than 1.5 km s^{-1} , and outside the central $0.2 r_{25}$ radial range.

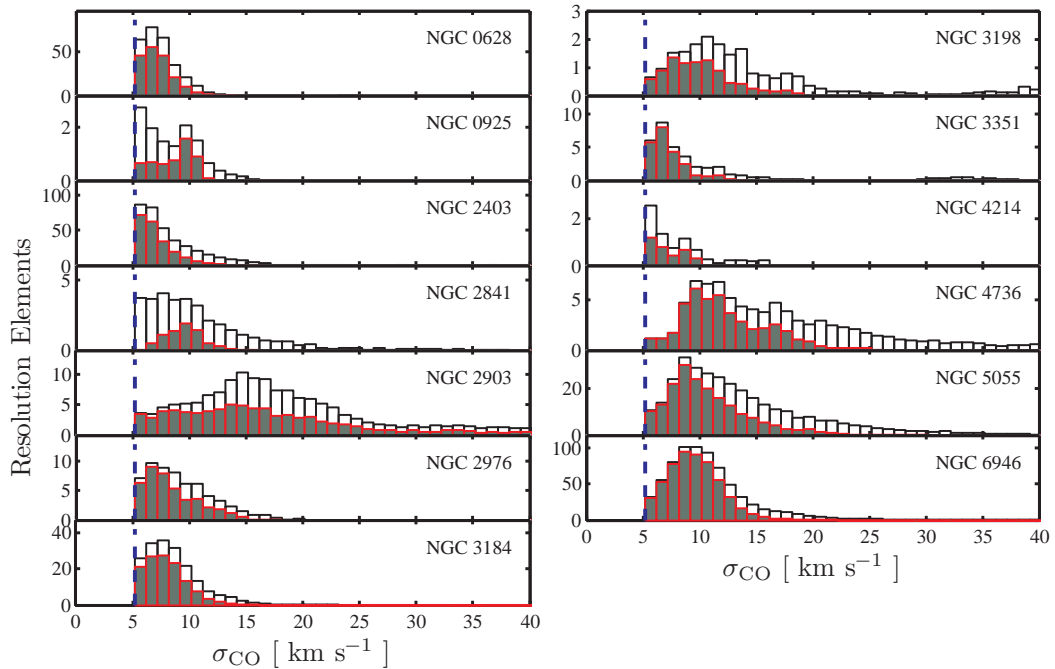


FIG. 3.— Same as Figure 2, but now for CO dispersions.

TABLE 2
THE STATISTICAL PROPERTIES OF THE H I AND CO DISPERSIONS.

Galaxy	σ_{CO} (km s^{-1})	σ_{HI} (km s^{-1})	σ_{HI} (all HI) (km s^{-1})	$\sigma_{\text{CO}} - \sigma_{\text{HI}}$ (km s^{-1})	$\sigma_{\text{CO}} - \sigma_{\text{HI}}$ (km s^{-1})	$\sigma_{\text{HI}}/\sigma_{\text{CO}}$	
(1)	(2)	(3)	(4)	(5)	(6)	(7)	(8)
NGC 628	6 (7.5)	9 (9.1)	6 (6.5)	-1.70 (± 0.04)	-2 (-1.6)	1.2 (± 0.01)	1.2 (1.3)
NGC 925	6 (8.5)	11 (13.2)	10 (10.9)	-3.5 (± 0.3)	-3 (-4.7)	1.4 (± 0.04)	1.3 (1.7)
NGC 2403	6 (8.3)	10 (12.3)	7 (8.7)	-3.8 (± 0.1)	-4 (-4.0)	1.5 (± 0.02)	1.4 (1.6)
NGC 2841	8 (10.9)	10 (18.0)	9 (15.5)	-3.5 (± 0.9)	-3 (-7.1)	1.3 (± 0.06)	1.3 (2.0)
NGC 2903	15 (21.6)	22 (25.3)	8 (12.1)	-5.5 (± 0.2)	-5 (-3.7)	1.3 (± 0.02)	1.2 (1.4)
NGC 2976	6 (9.3)	11 (12.2)	11 (13.2)	-3.1 (± 0.2)	-5 (-2.9)	1.3 (± 0.05)	1.1 (1.4)
NGC 3184	8 (8.6)	10 (11.1)	7 (8.3)	-2.57 (± 0.03)	-2 (-2.5)	1.3 (± 0.02)	1.2 (1.4)
NGC 3198	11 (15.0)	17 (20.2)	11 (12.5)	-6.6 (± 0.4)	-5 (-5.2)	1.4 (± 0.06)	1.2 (1.6)
NGC 3351	7 (14.1)	9 (18.9)	7 (9.8)	-2.8 (± 0.3)	-3 (-4.7)	1.4 (± 0.04)	1.2 (1.5)
NGC 4214	6 (8.0)	16 (14.0)	6 (7.4)	-6.0 (± 0.2)	-6 (-5.8)	1.4 (± 0.04)	1.6 (1.9)
NGC 4736	10 (17.7)	15 (23.5)	7 (10.4)	-3.4 (± 0.1)	-4 (-3.2)	1.2 (± 0.02)	1.0 (1.2)
NGC 5055	9 (14.9)	11 (17.9)	7 (9.9)	-2.9 (± 0.1)	-3 (-3.0)	1.2 (± 0.01)	1.3 (1.3)
NGC 6946	9 (11.6)	13.0 (13.5)	7 (8.4)	-2.4 (± 0.1)	-2 (-2.0)	1.2 (± 0.02)	1.2 (1.3)

NOTE. — These values were calculated for all pixels where both the H I and CO are above the noise cutoff, except for column 4 which was calculated for all pixels where the H I was above the noise cutoff. Column 1: Galaxy name; Column 2: Mode (mean) of CO dispersions; Column 3: Mode (mean) of H I dispersions; Column 4: Mode (mean) of H I dispersions of the entire H I disk; Column 5: Gaussian fitted mean (fit uncertainty) of $\sigma_{\text{CO}} - \sigma_{\text{HI}}$; Column 6: Mode (mean) of $\sigma_{\text{CO}} - \sigma_{\text{HI}}$; Column 7: Gaussian fitted mean (fit uncertainty) of $\sigma_{\text{HI}}/\sigma_{\text{CO}}$; Column 8: Mode (mean) of $\sigma_{\text{HI}}/\sigma_{\text{CO}}$.

TABLE 3
 THE MEAN, MODE AND MEDIAN DISPERSION VALUES

	σ_{CO} (km s^{-1})	σ_{HI} (km s^{-1})	$\sigma_{\text{CO}} - \sigma_{\text{HI}}$ (km s^{-1})	$\sigma_{\text{HI}}/\sigma_{\text{CO}}$
mode	7.3 ± 1.7	11.7 ± 2.3	-3.4 ± 1.4	1.3 ± 0.2
mean	10.5 ± 3.6	14.1 ± 4.3	-3.3 ± 1.4	1.4 ± 0.2
median	9.5 ± 3.0	13.1 ± 3.0	-3.3 ± 1.2	1.4 ± 0.2
fitted mean	-	-	-3.3 ± 1.2	1.4 ± 0.2

NOTE. — The values were calculated by taking the average of the modes, means, medians, and fitted means calculated for each galaxy in our sample. NGC 2841, NGC 2903, NGC 3198 and NGC 3351 were not included due their high inclinations and/or very asymmetric dispersion distributions. The fitted mean was not calculated for the HI and CO distributions because Gaussian profiles were not fitted to these distributions.

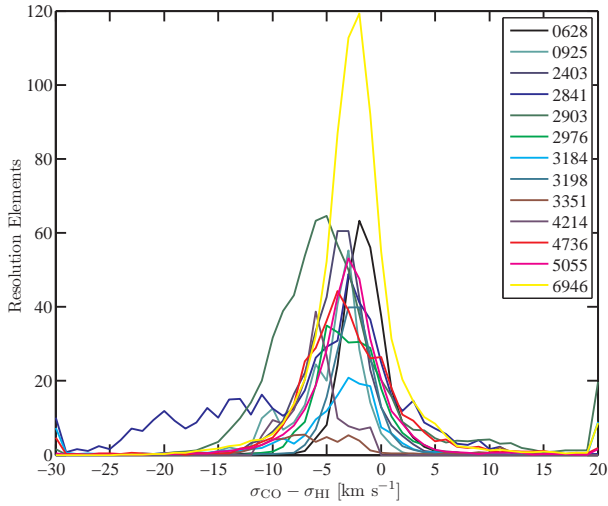


FIG. 4.— Distributions of the dispersion difference $\sigma_{\text{CO}} - \sigma_{\text{HI}}$ values of the galaxies. The lines are colour-coded by galaxy (see legend). The y-axis is in resolution elements (resolution elements = [number of pixels]/[number of pixels per single resolution element]). Values for NGC 925, NGC 2841, NGC 2903, NGC 3198, NGC 3351, NGC 4214 and NGC 4736 are multiplied by a factor of 5 for better comparison with the other galaxies.

 TABLE 4
 DISPERSION VALUES IN KM S^{-1} FOR $r > 0.2r_{25}$

	4S	8S	Stacking
	1	2	3
σ_{CO} mean	9.3 ± 2.1	8.9 ± 2.1	12.8 ± 3.9
σ_{CO} median	8.6 ± 1.8	8.4 ± 2.0	12.0 ± 3.9
σ_{HI} mean	12.7 ± 2.1	12.3 ± 2.3	12.7 ± 3.1
σ_{HI} median	12.2 ± 1.9	11.9 ± 2.1	11.9 ± 3.1
$\sigma_{\text{HI}}/\sigma_{\text{CO}}$ mean	1.5 ± 0.2	1.5 ± 0.3	1.0 ± 0.2

NOTE. — The mean and median dispersion values determined for pixels at $r > 0.2r_{25}$. Column 1: Using 4S noise cutoff. Column 2: Using 8S noise cutoff. Column 3: Values from stacking analysis from Caldú-Primo et al. (2013).

This behaviour was already seen in HI by Tamburro et al. (2009). The $\sigma_{\text{HI}}/\sigma_{\text{CO}}$ values remain roughly constant for most of the radial range covered; this can be seen in Fig. 7.

4. COMPARISON WITH STACKING RESULTS

We now compare our results with the stacking analysis by Caldú-Primo et al. (2013). In that study, which used the same data sets as the ones used here, the stacking

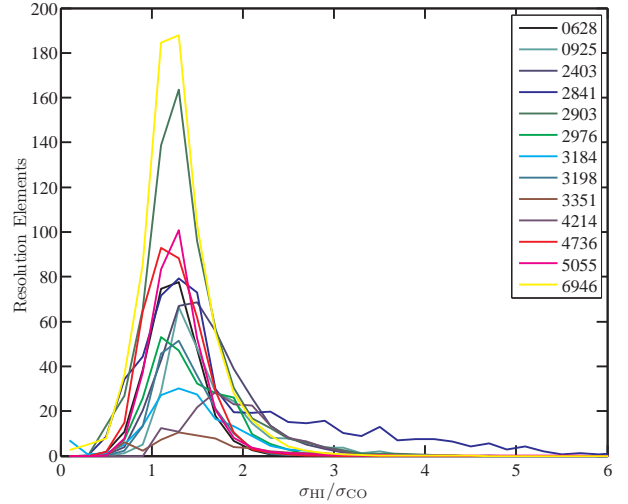


FIG. 5.— Distributions of the dispersion ratios $\sigma_{\text{HI}}/\sigma_{\text{CO}}$ of the galaxies for individual resolution elements. The y-axis is in resolution elements (resolution elements = [number of pixels]/[number of pixels per single resolution element]). Values for NGC 925, NGC 2841, NGC 2903, NGC 3198, NGC 3351, NGC 4214 and NGC 4736 are multiplied by a factor of 5 for better comparison with the other galaxies.

procedure included all possible CO profiles, i.e., there was no rejection based on CO peak-flux and all positions where an HI velocity was available for use in stacking the CO profile were used. The only profiles excluded from their analysis were those at radii less than $0.2r_{25}$. The mean and median dispersion values they found are shown in Table 4. These σ_{CO} values are higher than our mean and median values.

To check whether this difference is not caused by the higher uncertainties associated with low peak-flux profiles, we rederived our values for a number of different noise cutoffs between 4S and 8S. Our mean and median dispersion values for data with the central $0.2r_{25}$ pixels removed and using 4S and 8S noise cutoffs are shown in Table 4. Our pixel-by-pixel σ_{CO} values are lower irrespective of which noise cutoff we use. Our σ_{HI} values remain similar to the Caldú-Primo et al. (2013) values.

Due to the noise cutoff used here, our analysis does not probe the low peak-flux regime that the stacking analysis in Caldú-Primo et al. (2013) is sensitive to. It is therefore possible that the difference found in dispersion values could be caused by profiles with a peak flux lower than 4S having systematically higher velocity dispersions. It is, however, difficult to directly and accurately measure the individual velocity dispersions of these low peak-flux profiles.

We therefore evaluated the impact of the low peak-flux spectra by creating histograms of the velocity dispersion values for different noise cutoff values. If lower peak-flux profiles do indeed have higher velocity dispersions, then we would expect the fraction of high-dispersion profiles to decrease with increasing noise cutoff. In other words, the prominence of any high-dispersion tail in the histogram should decrease. For this analysis we used data from pixels with radii greater than $0.2r_{25}$. An example is shown in the top left panel of Fig. 8. Here we show the normalized σ_{CO} distributions for NGC 2403 derived using various noise cutoffs between 4S and 10S. It is clear that the distribution becomes more narrow with increasing cutoff

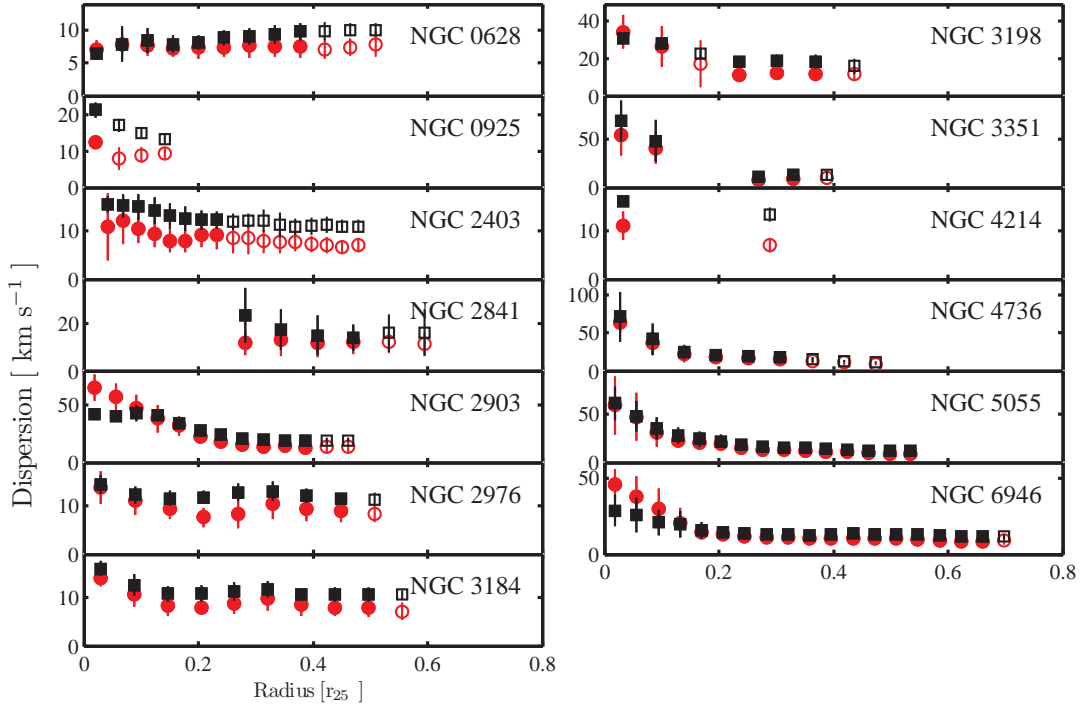


FIG. 6.— The azimuthally averaged σ_{CO} (red circles) and σ_{HI} (black squares) values plotted versus radius in each of the galaxies. The radius is in units of r_{25} . Azimuthal averages were taken over $13''$ annuli. Data from annuli where the CO has a filling factor of more than 10% are plotted as open symbols. Annuli where the filling factor is more than 25% are plotted as filled symbols. The error bars represent the standard deviation of the dispersion value in each annulus.

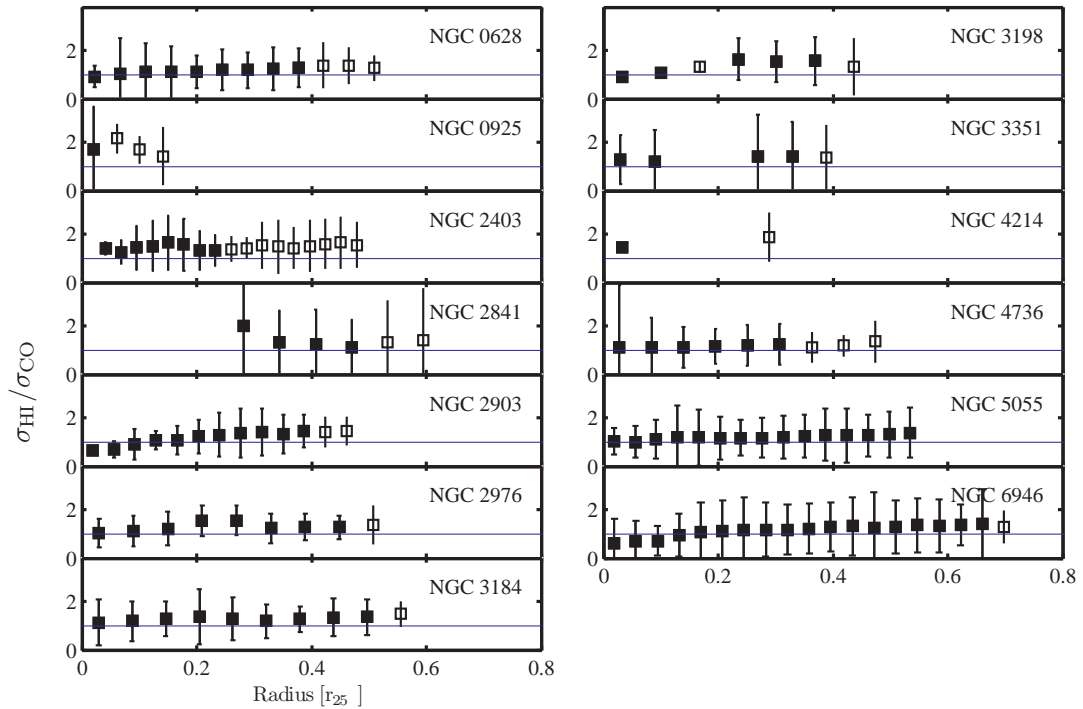


FIG. 7.— The $\sigma_{\text{HI}}/\sigma_{\text{CO}}$ ratio of the azimuthally averaged dispersions plotted versus radius in each of the galaxies. The radius is in units of r_{25} . Data from annuli where the CO has a filling factor of more than 10% are plotted as open symbols; data where the filling factor is more than 25% are plotted as filled symbols. The horizontal lines indicate $\sigma_{\text{HI}} = \sigma_{\text{CO}}$.

value. We quantify this with the histogram half-width at 20 percent of the maximum, where the half-width is measured in the direction of higher dispersions, with respect to the value of the histogram maximum (or the mode), as indicated in the left panel of Fig. 8. We have repeated this analysis for all our sample galaxies, except for NGC 925, NGC 4214 and NGC 3198, where CO emission is faint and limited in extent, and NGC 2903, where the dispersion values are dominated by streaming motions along the bar. We also excluded the central part of NGC 3351 which is dominated by a compact bar.

The top-right panel of Fig. 8 shows the values of the measured widths as a function of noise cutoff. For the majority of the galaxies shown there, the width becomes narrower toward higher cutoff values and the high-dispersion tail less prominent. We thus find that the fraction of high-dispersion spectra does indeed decrease with increasing peak flux and it is therefore likely that the low peak-flux profiles included in the stacking analysis (but excluded in ours) have systematically higher velocity dispersions.

This implies that repeating the stacking analysis of Caldú-Primo et al. (2013) with a *higher* noise cutoff should give *lower* dispersion values than their original analysis. We therefore performed a stacking analysis on our data using various cutoffs. As an example, in Figure 9 we show, as a function of radius, the difference between the 5*S* and the 8*S* stacked dispersions. The average difference between the dispersions is $\sim 1.5 \text{ km s}^{-1}$, independent of radius, with the 5*S* values systematically higher than the 8*S* ones.

To test whether the trend in velocity dispersion we found is not caused by the increasing importance of the noise toward lower peak fluxes (which might be expected to broaden profiles), we repeat our analysis using simulated profiles. We created Gaussian profiles with peak values between 4*S* and 10*S*, and with dispersions chosen with a probability distribution equal to the observed σ_{CO} distribution of NGC 2403, as shown in Fig. 3 (for pixels with radii greater than $0.2 r_{25}$). We explicitly assume that the velocity dispersion is independent of the peak flux. We compare the dispersion distributions found at various peak-flux levels in Figure 8 (bottom left). The change in these distributions is very different from that as observed for NGC 2403, as shown in the bottom right panel in Figure 8. The higher velocity dispersions measured at low peak flux are therefore not due to noise affecting the profiles, but due to an increase of the velocity dispersion toward lower peak fluxes.

A similar anti-correlation, but for HI rather than CO, was found for a number of dwarf galaxies by Hunter et al. (2001, 2011). Hunter et al. (2011) suggest that this anti-correlation is roughly consistent with a uniform pressure throughout these galaxies, as also found in simulations of magneto-rotational instabilities by Piontek & Ostriker (2005).

Returning to the observed CO velocity dispersions, Caldú-Primo et al. (2013) note that the higher dispersion values that are found in the stacked profiles can be explained with a diffuse, extended molecular gas component that pervades our galaxies in addition to the molec-

ular gas in GMCs in the thin, “cold” CO disk. Our pixel-by-pixel analysis is limited to pixels with bright CO emission, which is dominated by the GMCs. These velocity profiles are narrower than those dominated by emission from the diffuse CO disk.

These differences therefore are further evidence that a diffuse, high-dispersion component of molecular gas is present in our galaxies in addition to a thin molecular disk. The diffuse component of molecular disks may thus be a common feature in disk galaxies.

5. SUMMARY

We have measured the velocity dispersions in individual HI and CO profiles of a number of THINGS disk galaxies. We find an HI velocity dispersion of $\sigma_{\text{HI}} = 11.7 \pm 2.3 \text{ km s}^{-1}$. The corresponding CO value is $\sigma_{\text{CO}} = 7.3 \pm 1.7 \text{ km s}^{-1}$. The ratio between these two dispersions is $\sigma_{\text{HI}}/\sigma_{\text{CO}} = 1.4 \pm 0.2$ and is not correlated with radius.

In a previous study using the same data, Caldú-Primo et al. (2013), by stacking individual velocity profiles, found a systematically higher CO velocity dispersion and a ratio $\sigma_{\text{HI}}/\sigma_{\text{CO}} = 1.0 \pm 0.2$. This difference can be explained if low peak-flux CO profiles have a systematically higher velocity dispersion than high-peak flux profiles. Our pixel-by-pixel analysis preferentially selects the bright, high peak-flux CO profiles, in contrast with the stacking analysis which also includes large numbers of low peak-flux CO profiles.

The relation of σ_{CO} decreasing with increasing profile amplitude is consistent with a picture where the bright CO regions (preferentially selected in studies of individual profiles) are dominated by narrow-line GMCs, with a more diffuse, higher dispersion component (more efficiently detected in stacking analyses) becoming more prominent toward lower intensities. A pixel-by-pixel analysis is therefore a good way to study the thin molecular disk component where GMCs dominate the emission. In turn, stacking analyses are more sensitive to the diffuse, high-dispersion extended molecular disk component.

Our results thus provide further evidence for the suggestion presented in Caldú-Primo et al. (2013) that many disk galaxies have an extended, diffuse molecular disk component in addition to a thin, GMC-dominated, molecular disk.

We gratefully thank the anonymous referee for all the comments and suggestions that improved the content of the paper. K.M.M. gratefully acknowledges support from the Square Kilometre Array South Africa (SKA-SA) and the National Astrophysics and Space Science Program (NASSP). K.M.M. would like to thank S. Schutte for the useful discussions during the preparation of the manuscript. The work of W.J.G.d.B. was supported by the European Commission (grant FP7-PEOPLE-2012-CIG #333939). R.I. acknowledges funding from the National Research Foundation (NRF grant number MWA1203150687) and the University of South Africa (UNISA) postdoctoral grant.

Facilities: IRAM 30m, VLA.

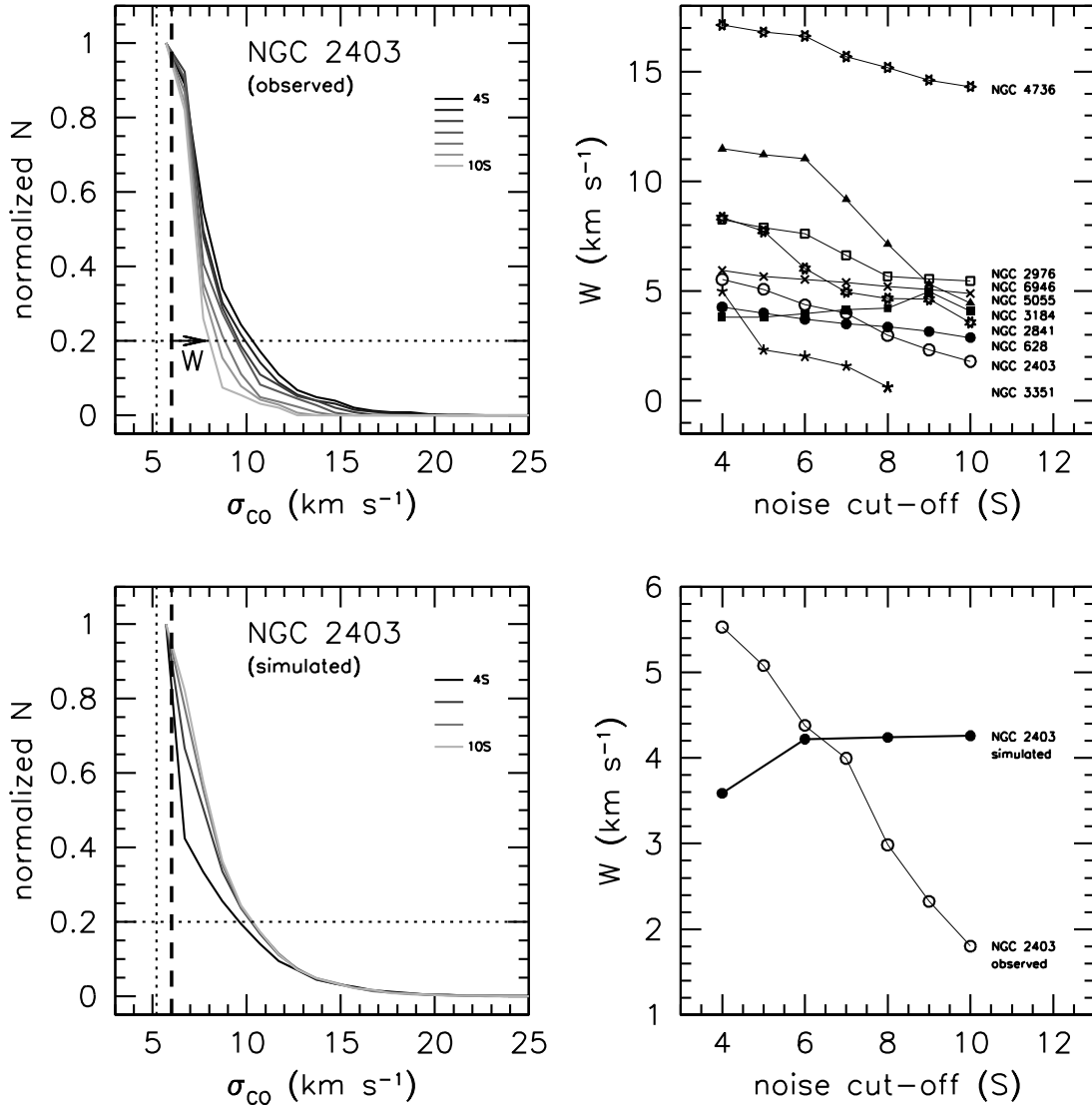


FIG. 8.— *Top Left*: normalized distributions of σ_{CO} for NGC 2403 for different values of the noise cutoff. The black curve indicates a 4S cutoff. From black to light gray, the noise cutoff increases in steps of S with the light-gray curve indicating a 10S cutoff. It is clear that the curves become narrower with increasing noise cutoff. The thick dashed vertical line indicates the mode of the distribution, the dotted vertical line the velocity resolution cutoff. The horizontal dotted line indicates the 20 percent level at which the width with respect to the mode is measured. The width W is indicated for the 10S curve by the arrow labelled “W”. *Bottom Left*: normalized distributions of the simulated NGC 2403 data for different peak-flux values. Velocity profiles were simulated with random noise, varying input amplitudes, and input dispersions drawn from NGC 2403’s 4S σ_{CO} distribution. The profiles were fitted in the same manner as the observed data and the histograms of the fitted dispersions are plotted. *Top Right*: the 20 percent width W as defined in the left panel plotted against the noise cutoff in units of S . Galaxies are labeled to the right of their corresponding curve. Note that for NGC 3351 only values up to 8S could be measured. *Bottom Right*: the W values of the observed NGC 2403 σ_{CO} distributions and the simulated distributions are plotted against the modeled peak-flux value.

APPENDIX

COMPARING H I VELOCITY DISPERSIONS AND SECOND MOMENTS

In a previous study, Tamburro et al. (2009) determined the second moments of the H I profiles of the THINGS galaxies as an estimate for the velocity dispersions. These second moments were measured as a function of radius over the full extent of the H I disk.

To gauge how well the second-moment values match the Gaussian dispersion values σ_{HI} , we derive both parameters for our H I profiles, as also measured over the entire radial range and full area of the H I disk, i.e., also including regions without CO emission.

Figure 10 shows that there are some slight differences in the second-moment values and Gaussian fitted dispersions. For most galaxies the largest differences between second-moment values and Gaussian fitted dispersions are found in the inner regions of galaxies, with second-moment values being larger than the Gaussian fitted dispersions. The inner regions of the galaxies have more non-Gaussian profiles than the outer regions. This shows that the second moment is more sensitive to non-Gaussianities than profile fits and in these cases should be interpreted with care.

We note that the H I dispersions associated with the CO disk (the inner star-forming disk) are higher than the

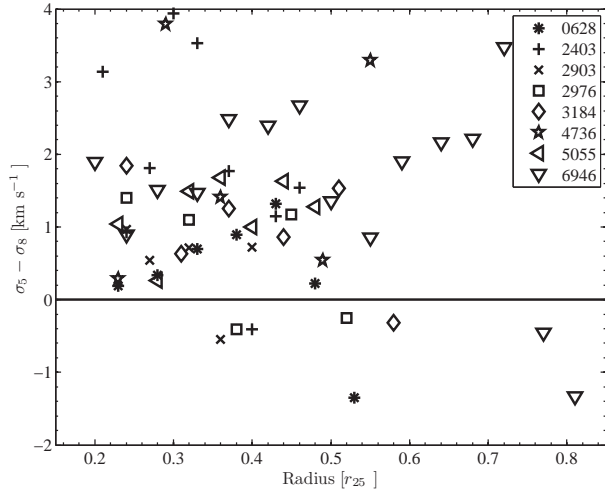


FIG. 9.— Differences between the stacked mean σ_{CO} dispersion calculated for profiles with peak flux $> 8S$ (σ_8) and $> 5S$ (σ_5) plotted against radius.

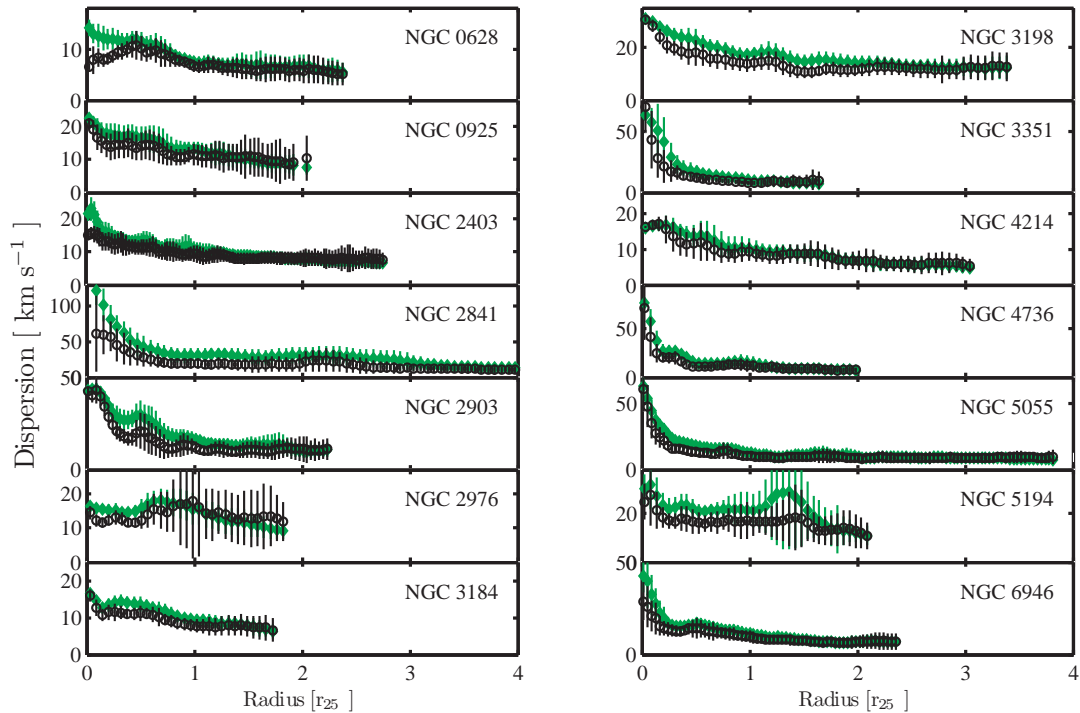


FIG. 10.— Azimuthally averaged σ_{HI} values plotted versus radius in each of the galaxies. The radius is in units of r_{25} . Azimuthal averages were taken over $13''$. The error bars represent the standard deviation of the dispersion values in each annulus. The black open circles are Gaussian fitted dispersions and the green filled diamonds are second-moment dispersions. Only annuli with filling factors above 10% are shown.

dispersion as measured over the entire HI disk (which includes the outer parts of the galaxy where there is no detectable CO). This can be explained by the higher star formation rate in the inner disk compared to the outer disk. A further discussion of this is, however, beyond the scope of this paper.

REFERENCES

- Agertz, O., Lake, G., Teyssier, R., et al. 2009, MNRAS, 392, 294
 Caldú-Primo, A., Schruba, A., Walter, F., et al. 2013, AJ, 146, 150
 Caldú-Primo, A., Schruba, A., Walter, F., et al. 2015, AJ, 149, 76
 Combes, F., & Becquaert, J.-F. 1997, A&A, 326, 554
 Combes, F., Boquien, M., Kramer, C., et al. 2012, A&A, 539, 67
 de Blok, W.J.G., Walter, F., Brinks, E., et al. 2008, AJ, 136, 2648
 Elmegreen, B.G. 1989, ApJ, 338, 178
 Garcia-Burillo S., Guelin, M., Cernicharo, J., et al. 1992, A&A, 266, 21
 Hunter, D.A., Elmegreen, B.G., Oh, S., et al. 2011, AJ, 142, 121
 Hunter D.A., Elmegreen, B.G., & van Woerden, H. 2001, ApJ, 556, 773

- Ianjamasimanana, R., de Blok, W.J.G, Walter, F., et al., 2012, AJ, 144, 96
- Kamphuis, J., & Sancisi, R. 1993, A&A, 273, 31
- Kennicutt, R.C. 1989, ApJ, 344, 658
- Krumholz, M.R., & McKee, C.F. 2005, ApJ, 630, 250
- Larson, R.B. 1981, MNRAS, 194, 809
- Leroy, A.K., Walter, F., Bigiel, F., et al. 2009, AJ, 137, 4670
- Leroy, A.K., Walter, F., Brinks, E., et al., 2008, AJ, 136, 2782
- Petric, A.O., & Rupen, M.P. 2007, ApJ, 134, 1952
- Pety, J., Schinnerer, E., Leroy, A.K., et al. 2013, ApJ, 779, 43
- Piontek, R.A., & Ostriker, E.C 2005, ApJ, 629, 849
- Shetty R., Clark, P.C., & Klessen, R.S. 2014, MNRAS, 442, 220
- Shostak, G.S., & van der Kruit, P.C. 1984, A&A, 132, 20
- Stark, A.A. 1984, ApJ, 339, 763
- Stilp, A. M., Dalcanton, J. J., Warren, S. R., et al. 2013, ApJ, 765, 136
- Tamburro, D., Rix, H.-W., Leroy, A.K., et al. 2009, AJ, 137, 4424
- Toomre, A. 1964, ApJ, 139, 1217
- van der Kruit, P.C., & Shostak, G.S 1984, A&A, 134, 258
- Walsh, W., Beck, R., Thuma, G., et al. 2002 A&A, 388, 7
- Walter, F., Brinks, E., de Blok, W.J.G., et al., 2008, AJ, 136, 2563
- Wilson, C.D., Warren, B.E., Irwin, J., et al. 2011, MNRAS, 410, 1409
- Wilson, C.D. & Scoville, N. 1990, ApJ, 363, 435